HHS Public Access
Author manuscript
Adv Healthc Mater. Author manuscript; available in PMC 2024 July 01.

Published in final edited form as:
Adv Healthc Mater. 2023 July ; 12(19): e2202619. doi:10.1002/adhm.202202619.

Fractal microelectrodes for more energy-efficient cervical vagus nerve stimulation

Jongcheon Lim[1,2,3], **Calvin D. Eiber**[4,5,†], **Anina Sun**[6], **Amanda Maples**[1], **Terry L. Powley**[1,7,8], **Matthew P. Ward**[1,9,*], **Hyowon Lee**[1,2,3,*]

[1]Weldon School of Biomedical Engineering, Purdue University, West Lafayette, IN, USA

[2]Birck Nanotechnology Center, Purdue University, West Lafayette, IN, USA

[3]Center for Implantable Devices, Purdue University, West Lafayette, IN, USA

[4]Synchron Inc., Melbourne, Victoria, Australia

[5]Department of Medicine (RMH), Faculty of Medicine, Health and Dentistry, The University of Melbourne, Melbourne, Victoria, Australia

[6]Department of Biology, Purdue University, West Lafayette, IN, USA

[7]Department of Psychological Sciences, Purdue University, West Lafayette, IN, USA

[8]Purdue Institute of Integrative Neuroscience, Purdue University, West Lafayette, IN, USA

[9]Indiana University School of Medicine, Indianapolis, IN, USA

Abstract

Vagus nerve stimulation (VNS) has the potential to treat various peripheral dysfunctions, but the traditional cuff electrodes for VNS are susceptible to off-target effects. Microelectrodes may enable highly selective VNS that can mitigate off-target effects, but they suffer from increased impedance. Recent studies on microelectrodes with non-Euclidean geometries have reported higher energy-efficiency in neural stimulation applications. These previous studies used electrodes with mm/cm-scale dimensions, mostly targeted for myelinated fibers. Our study evaluated fractal microelectrodes for VNS in a rodent model (N=3). We fabricated a thin-film device with fractal and circle microelectrodes to compare their neural stimulation performance on the same radial coordinate of the nerve. Our results show that fractal microelectrodes can activate C-fibers with up to 52% less energy ($p = 0.012$) compared to circle microelectrodes. To the best of our knowledge, our work is the first to demonstrate a geometric advantage of fractal microelectrodes for VNS *in vivo*.

Graphical Abstract

*Co-corresponding Author: mpward@purdue.edu, hwlee@purdue.edu.
†Disclosure: Dr. Calvin D. Eiber is a full-time employee of Synchron, Inc. Synchron was not involved in any aspect of the study (funding for the study; design and conduct of the study; collection, management, analysis interpretation of the data; preparation of the manuscript, or the decision to submit the manuscript for publication)

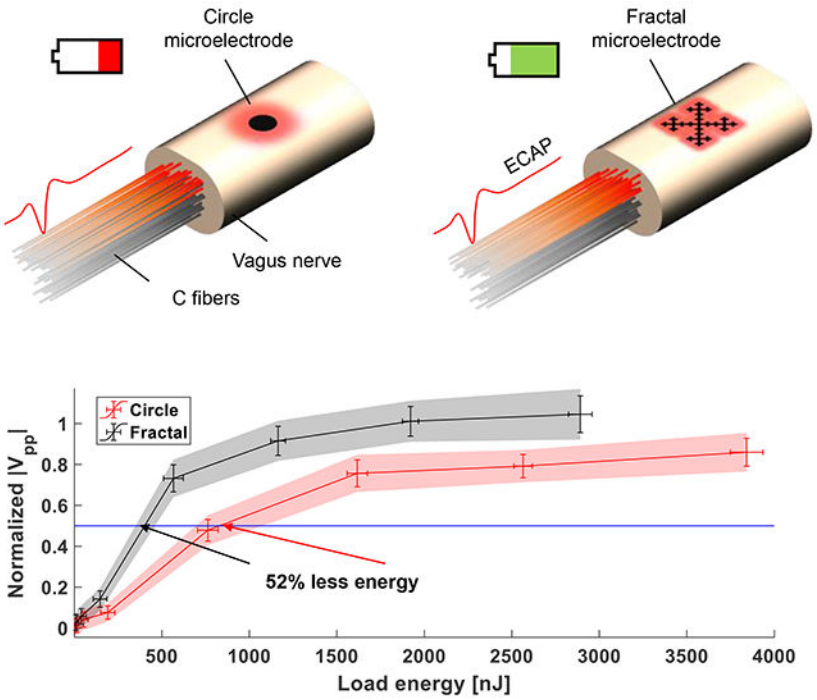

Microelectrodes can be used to increase neurostimulation selectivity. However, smaller electrodes have higher impedance, which can affect neurostimulation efficiency. This study presents an in vivo evaluation of microelectrodes with circular or fractal geometries. The findings suggest that fractal microelectrodes consume 52% less energy than circular microelectrodes in activating unmyelinated C-fibers in the Vagus nerve. Moreover, the activation threshold is lowered with fractal microelectrodes.

Keywords

Fractal; Microelectrode; Vagus Nerve Stimulation

Introduction

Vagus nerve stimulation (VNS) is a device-based therapy that electrically stimulates the vagus nerve to treat drug-resistant neurological disorders like epilepsy[1,2], depression[3], and migraine/cluster headache[4]. VNS is also known to be able to attenuate the systemic inflammatory response to endotoxin[5]; hence it can potentially work as an emerging treatment for Rheumatoid arthritis[6] and Crohn's disease[7]. Other previous pre-clinical studies have also shown that VNS has the potential to treat other peripheral disorders such as heart failure[8] and gastroparesis[9]. Multiple organs including the heart, lungs, laryngopharynx, and gastrointestinal tract relay sensory information via vagal afferent fibers[10], which comprise about 80% of the nerve fibers in the vagus nerve[11,12]. Vagal efferent fibers relay reflex motor signals to regulate parasympathetic activities of the organs[10]. Vagal afferents and efferents are predominantly unmyelinated fibers, and the majority of them are C-fibers[10,11]. Typically, VNS systems use helical cuff electrodes with a large surface area to cover

approximately three-quarters of the circumference of the cervical vagus nerve[13]. Helical cuff electrodes stimulate the entire nerve bundle indiscriminately, resulting in off-target effects. Commonly reported off-target effects include coughing, hoarseness, voice alteration, and paresthesia[14]. Microelectrodes have the potential to selectively stimulate specific nerve bundles with vagus to avoid off-target effects (Figure 1a) due to their higher spatial resolution.

Several studies have investigated the possibility of selective stimulation of nerve fibers (see Table 1). Tyler *et al.* (2002) developed a flat interface nerve electrode (FINE) that enabled a spatially selective stimulation of the sciatic nerve[15], tibial and common peroneal nerves[16], and femoral nerve[17]. More recently, Aristovich *et al.* (2021) studied an optimized design of a multi-contact electrode array for spatially selective stimulation of the cervical vagus nerve in a sheep model[18]. Although these works show the possibility of selective nerve stimulation, they used relatively larger electrodes (~1 mm^2), which limits spatial resolution. The use of a smaller microelectrode with a smaller geometric surface area (GSA) may be able to provide superior spatial selectivity with a higher-density array. However, decreasing the GSA results in higher interfacial impedances[19,20] which can lead to a higher energy requirement for stimulation. Power management is a critical issue for the reliable long-term operation of implantable neurostimulation systems. The battery life of the implantable pulse generator (IPG) used in neurostimulation systems ranges between 3 to 6 years, depending on multiple factors such as battery type, stimulus parameters, and the number of channels[21]. Microelectrodes typically have a higher impedance[20] and require a higher potential for the same pulse current amplitude, which decreases IPG battery life.

There is a large body of literature that has explored ways to reduce electrode interface impedance[22–34]. Many of these attempts can be categorized into either material-based[22–28] vs. geometry-based solutions[29–35]. Although platinum (Pt) is regarded as the gold standard for neurostimulation, various other materials for neural stimulation and recordings have been explored including titanium nitride (TiN)[22,23], iridium oxide (IrOx)[24,25], Pt-black, and conductive polymers like poly(3,4-ethylenedioxythiophene) (PEDOT)[26,27]. Among these candidates, Pt-black – electroplated Pt with roughened nanoscale morphology – is relatively accessible in a general laboratory environment and is used frequently to lower the interfacial impedance of microelectrodes[28].

In terms of geometry-based solutions, previous studies have predicted that electrodes with a higher perimeter-to-surface-area ratio (PSA) can provide a nominal performance improvement of neural stimulation by decreasing access resistance at the electrode-electrolyte interface. Golestanirad *et al.* (2013) investigated the section modified Sierpinski carpet fractal electrode *in silico* by evaluating the power efficiency in transcutaneous stimulation of the human median nerve[29]. The study highlights a 22% power reduction at 50% activation of the median nerve by using the fractal electrode compared to a simple square electrode; however, this simulation was based on centimeter-scale electrodes for transcutaneous charge injection[29]. Park *et al.* (2018) evaluated a microelectrode with Vicsek fractal geometry in terms of electrochemical characterization and concluded that the fractal microelectrode outperforms the circle microelectrode saving energy by 47% due to the fractal microelectrode's improved diffusion capabilities, lower charge transfer

resistance, lower access resistance, and a higher double layer charging[30]. Several others demonstrated similar performance benefits of non-Euclidean geometry electrodes using various computational and in vitro experiments[31–34].

Only a handful of studies have conducted *in vivo* experiments to evaluate electrodes with non-Euclidean shapes[29,35]. Howell and Grill studied high-perimeter electrodes with "Serpentine-edge" and "Square-edge (Rook)" designs for deep brain stimulation (DBS) in a feline model. They compared the energy efficiency of the millimeter-scale electrode with different GSA and PSA ratio but did not directly compare the efficiency between different types of shapes[35]. To the best of our knowledge, there have not been any *in vivo* studies to evaluate the performance of non-Euclidean microelectrodes.

Here we compared the electrical stimulation performance of circular versus fractal microelectrodes in a rat Vagus nerve (Figure 1b). We implemented a polyimide (PI) based thin-film device with circular and fractal designs to evaluate the effect of microelectrode shape on C fiber recruitment in a rat cervical vagus nerve. Our results suggest that fractal geometry can be leveraged to decrease the overall impedance of microelectrodes and improve the charge injection capacity of these neurostimulation electrodes as predicted *in silico* and *in vitro*.

Results

Electrochemical characterization of microelectrodes on the thin-film device

To evaluate the performance of each microelectrode, we conducted electrochemical characterizations including cyclic voltammetry (CV), electrochemical impedance spectroscopy (EIS), and voltage transient in phosphate buffered saline (PBS) solution. Figure 2a shows a representative result from CV measurements of the circle (red trace) and the fractal (black trace) electrode with and without Pt-black coating. We calculated the cathodic charge storage capacity (CSC_c) from the total charge storage capacity (CSC) of the voltammograms using the following equation[36]:

$$CSC = \frac{1}{\nu A}\int_{E_c}^{E_a} |i| dE \tag{1}$$

with the potential versus Ag/AgCl reference electrode E, measured current i; the positive and negative potential limits E_a and E_c respectively; surface area of the microelectrode A; the scan rate ν. Only the cathodic current was used for the calculation of CSC_c. Figure 2b shows the comparison of CSC_c of the circle (3.6 ± 0.2 mC cm^{-2}) and the fractal (4.3 ± 0.2 mC cm^{-2}) microelectrodes, which indicate that the fractal electrodes have 18% higher CSC_c compared to circle microelectrodes (N=4, ANOVA Tukey's HSD post hoc analysis, $p < 0.01$). This result is following the trend in the previous works of Park *et al.* (2018)[30,37] that fractal microelectrode yields higher CSC_c compared to circle microelectrode. After Pt-black coating, the absolute value of CSC_c increased 15 times for the circle (53 ± 2.6 mC cm^{-2}) and fractal (66 ± 2.0 mC cm^{-2}) compared to the results from bare Pt: The CSC_c for Pt-black coated fractal is 25% higher than the circle.

We conducted EIS to check the performance of the microelectrodes in terms of their impedance Figure 2c shows representative Bode impedance plots from the EIS of the circle and the fractal microelectrodes. The impedance of fractal microelectrode with bare Pt surface at 1 kHz was lower (38 ± 1.0 kΩ) compared to that of circle electrode (73 ± 1.4 kΩ), which was also expected based on our previous work[30,37]. The trend also remained after Pt-black coating: the impedance of the fractal at 1 kHz was lower (2.4 ± 0.02 kΩ) than that of the circle (3.6 ± 0.03 kΩ).

To identify the charge injection limit profiles of fractal and circle electrodes, we measured the voltage transient response of each electrode. Figure 3a shows a representative plot that shows voltage drops of microelectrodes in PBS solution (pulse current amplitude = 0.3 mA, pulse width = 0.5 ms). We estimated the negative maximum potential excursion E_{mc} for each type of electrode (N=4) as the electrical potential at the end of the current pulse (blue line in Figure 3a). Figure 3b shows the average E_{mc} of the circle and the fractal microelectrodes with bare Pt or Pt-black surface. For the bare Pt surface, pulse current amplitudes of 0.011 mA and 0.016 mA resulted in E_{mc} = −0.6 V in the circle and fractal microelectrodes, respectively. After Pt-black coating, pulse amplitudes increased to 0.32 mA for circle and 0.37 mA for fractal (Figure 3b). Using these values along with GSA of the microelectrode (7854 μm^2 for both circle and fractal) and pulse duration (0.5 ms), we estimated the charge injection limit: Charge injection limit = Pulse current amplitude at −0.6 V of E_{mc} X pulse duration / GSA. Pt-black coating improved charge injection limit of circle microelectrodes from 0.07 mC cm^{-2} to 2.05 mC cm^{-2} (29 times higher); fractal from 0.10 mC cm^{-2} to 2.36 mC cm^{-2} (24 times higher). The estimated charge injection limit of Pt-black coated fractal microelectrodes is 15% higher than equivalent circle microelectrodes.

To compare the energy efficiency between different electrodes, we calculated load energy (E_{load}) from the voltage transient measurement using the following equation [38]:

$$E_{load} = \int_0^{PW} I_{stim} V_{load} dt \tag{2}$$

Where PW is the pulse duration, I_{stim} is the pulse current amplitude and V_{load} is the load voltage. Figure 3c shows the load energy for different electrodes. For the comparison of load energy for bare Pt and Pt black, we set the maximum pulse current amplitude as 0.4 mA to prevent gas bubble generation from the surface of bare Pt electrodes. At 0.4 mA of pulse current amplitude, Pt-black coating improved load energy of circle microelectrodes from 720 ± 38 nJ to 360 ± 40 nJ (100 ± 19% reduction); fractal from 440 ± 19 nJ to 250 ± 25 nJ (72 ± 15% reduction): The Pt-black coated fractal microelectrodes consumed 40 ± 22% (p=0.0048) less energy compared to circle microelectrodes, which corresponds to the result (47% of energy saving) from Park *et al.* (2018)[30].

Comparison of ECAP waveforms evoked by different electrodes

Figure 4a–c shows mean ECAP waveforms elicited at the cathodic phases by conventional circumferential electrodes (Figure 4d), circle (Figure 4e), and fractal (Figure 4f) microelectrodes in one animal at different stimulus parameters. In all three electrodes, the

stimulation evoked ECAPs at the latency range from 5 ms to 15 ms above certain pulse current amplitudes (pulse duration = 1 ms). Conduction distances for the circumferential, circle, and fractal were 5.51 mm, 4.78 mm, and 4.38 mm, respectively in this experiment. We used the measured conduction distances to plot the ECAP with respect to conduction velocity. The estimated conduction velocities of the volleys were from 0.27 m s^{-1} to 1.0 m s^{-1}, which is in the range of the C-fiber conduction velocity (0.2-2 m s^{-1} [39]). Our latency range for the C-fiber activity (5-15 ms) from the stimulation with the circumferential cuff electrode (Figure 4d) is in agreement with a previously reported result from the rat model with a similar stimulation and recording setting[40]. The waveforms of the C-fiber ECAP volleys for circle and fractal microelectrodes are similar to the result from the circumferential electrode in terms of latency and shape (Figure 4d–f). The ECAP volleys at C-fiber's conduction velocity range have the shape of a diphasic waveform with a negative peak (N1) and a following positive peak (P1) for all three electrodes (Figure 4g–i).

Comparison of activation profiles and load energy for circle and fractal microelectrodes

To evaluate the performance of the circle and the fractal microelectrodes in terms of their capability to recruit axon fibers and the energy efficiency, we visualized the recruitment profile of $|V_{pp}|$ of the C-fiber volleys with respect to load energy. Figure 5a–c show measured activation profiles for VNS using circle and fractal microelectrodes for each animal. The stimuli comprised 10 s train duration of 1 ms current-controlled pulses, 5 Hz of pulse repetition frequency alternating cathodic and anodic pulses: cathodic pulse for the charge injection and anodic pulse for the charge balancing. To mitigate the experimental variability in maximum $|V_{pp}|$ across animals, we normalized the $|V_{pp}|$ for microelectrodes to the maximum value for each animal and computed a grand mean (and 95% CI) across animals. The average normalized $|V_{pp}|$ profile from all three animals shows higher recruitment for fractal microelectrodes for pulse current amplitudes greater than 0.1 mA, but the 95% CI overlaps except for 0.4 mA and 0.8 mA (Figure 5d). However, the 50% activation levels of the normalized $|V_{pp}|$ for the circle and the fractal are placed in the range where their 95% CIs do not overlap, which indicates the significant difference of activation level at this current range.

We estimated pulse current amplitude (I_{50}), charge per phase (Q_{50}), and load energy at 50% activation of vagal C fibers by linearly interpolating the two data points immediately below and above the 50% activation level. The estimated I_{50} for fractal microelectrodes (I_{50} : 0.33 ± 0.02 mA, Q_{50} : 0.33 ± 0.02 μC) is 23% ± 17% smaller ($p = 0.021$) than for circle microelectrodes (I_{50} : 0.43 ± 0.06 mA, Q_{50} : 0.43 ± 0.06 μC). Fractal microelectrode VNS consumed 420 ± 53 nJ at 50% activation, 52% ± 33% less ($p = 0.012$) than with circle microelectrodes (880 ± 250 nJ). Figure 5e shows the profile of load energy estimated via the voltage transient experiment with the same stimulus parameter combinations used for the *in vivo* experiment. Figure 5f shows the plot of normalized $|V_{pp}|$ with respect to load energy for each stimulus amplitude. These data suggest that VNS with fractal microelectrodes is more efficient than with circle microelectrodes.

Analysis of computationally modeled nerve fibers

We simulated spatial distributions of thresholds for circle (Figure 6a) and fractal (Figure 6b) microelectrode VNS, using biophysical axon models with diameters derived from electron microscopy. Simulated VNS using circle microelectrodes yields lower thresholds for the nerve fibers near the center of the electrode (Figure 6a) relative to fibers further from the electrode. At thresholds higher than 0.1 mA, the contour for fractal shows wider recruitment of fibers (Figure 6b), relative to the circle. Figure 6c shows thresholds (pulse duration = 1 ms) for each model C-fiber axon in the nerve for fractal and circle in a scatter plot. Each marker indicates an axon in the nerve for both circle and fractal microelectrodes. The fitted line from linear regression (yellow line) and 95% CI (yellow shaded region) shows that, on average, circle microelectrodes recruit fewer fibers than fractal microelectrodes for stimuli above 0.12 mA (slope = 0.71). For this configuration of the vagus nerve and microelectrode array, 98.14% of axons have thresholds above 0.12 mA. Figure 6d shows recruitment profiles for the thresholds of C-fiber efferents and afferents for circle and fractal. Assuming 74% of the fibers are afferents[11], the thresholds of the fiber at 50% recruitment were 0.51 mA and 0.40 mA for circle and fractal, respectively. Fractal microelectrode VNS recruits 50% of modeled C-fibers with 19.75% less pulse current amplitude, closely replicating the observed recruitment with 23.26% less pulse current amplitude (and charge per phase) using fractal microelectrodes in our animal experiments.

Discussion

In this paper, we have shown that the Vicsek fractal microelectrode can evoke neural responses from the rat vagus nerve to a 50% activation level with less energy consumption compared to the circle microelectrode. The normalized ECAP recruitment profile shows that fractal microelectrodes consumed 52% ± 33 % ($p = 0.012$) less energy to activate 50% of maximum recruitable fibers (Figure 5f). To the best of our knowledge, this is the highest energy saving among similar previous works that evaluated various electrode designs (Table 2).

More C-fibers were recruited at equivalent pulse current amplitudes for fractal microelectrodes as compared to circle electrodes in our animal experiments (Figure 5a–c). These results correspond with the simulated recruitment profile (Figure 6d). The scatter plot of Figure 6c indicates that the thresholds for the circular microelectrodes are lower below 0.12 mA and become higher than fractal thereafter (Figure 6c), which suggests that circle microelectrode can focalize recruitment of a smaller number of fibers with lower current thresholds near the electrode, but fractal can recruit more fibers with same current amplitude. The footprint extent of the fractal microelectrode (157 μm) was greater than the circle microelectrode (100 μm), which likely affected the performance of axon activation; this will need to be investigated thoroughly in a future study along with different geometries. We believe that the shape of the microelectrode should be considered carefully depending on the spatial distribution of the target nerve fiber groups within the nerve for better spatial selectivity.

C-fibers are known to have an activation threshold 200× higher than A-fibers[41]. Activation of C-fibers requires the cautious choice of stimulus parameter combination, which can easily

exceed the safety limits imposed by the electrode material[42]. Previously, Park et al. (2018) have shown that the fractal microelectrode can inject more charge per phase than the circle microelectrode when the material is bare Pt[30]. Our work shows that this trend is preserved for Pt-black coated microelectrodes as well (Figure 3b). Although we were not able to find clear evidence that either fractal or circle microelectrodes can activate C-fiber activities to an observable magnitude in the measured ECAP within the charge injection limit (circle: 2.05 mC cm^{-2}; fractal: 2.36 mC cm^{-2}) since we observed the diphasic volley from 0.2 mA of pulse current amplitude for both microelectrodes (charge per phase: 2.55 mC cm^{-2}), we believe that the charge injection limit can be improved further by using different materials such as IrOx (3.9 mC cm^{-2})[43] and PEDOT:Nafion (4.4 mC cm^{-2})[44], or applying different stimulus waveforms[45,46]. We may not even have to inject the charge over the safety limit to activate a smaller portion of C-fibers, although it might not be observable in the macroscopic ECAP waveform measured by a cuff electrode. In this case, a more invasive intraneural measurement of nerve fiber activities using a Utah slanted electrode array (USEA) type of device might be necessary to investigate the spatially selective nerve fiber activation evoked by stimulating with the microelectrodes. Furthermore, the stimulus parameters can be tuned to lower magnitudes to target larger fibers which are relatively easier to modulate: Targeting B-fibers, which are related to heart rate[47]; A-fibers, which are related to breathing pattern[40].

Previous works in large animal models showed that ECAP signals from the vagus nerve may be contaminated by muscle activities that are evoked by the electric field generated from the helical cuffs that are implanted to the cervical vagus nerve[48,49]. We evaluated the contribution of muscle artifact in our rat model by transecting the superior laryngeal nerve (SLT), the caudal end of the vagus nerve (CT) to eliminate recurrent laryngeal nerve, and the transection between stimulation cuff site and recording cuff site (vagotomy) to eliminate the neural signals (Figure S5a–d). We used the same MicroLeads cuff electrodes that were used for the circumferential cuff stimulation experiment. We were able to observe the diphasic volleys between 10-20 ms latency range after SLT (Figure S5c) and SLT+CT (Figure S5d), and the volley disappears after the vagotomy (Figure S5e). This result suggests that the muscle artifact traveling in the surgical cavity filled with saline may not have significantly contributed to the diphasic volleys we observed in our experimental conditions. Additionally, in one experiment, we measured an electromyogram (EMG) signal from the larynx using a method introduced in a previous study[50] (see “2.6. Surgical procedure” part in the “Materials and Methods” section). For 1 mA of pulse current amplitude and 0.1 ms of pulse duration, myelinated fiber activities appear at the early latency region, but no clear C-fiber volleys were observable from the ECAP waveform (Figure S6d), whereas EMG signal appears at the latency earlier than 5 ms (Figure S6g). At a pulse duration of 0.4 ms, the C-fiber volley is clearly observable at the latency close to 10 ms with a conduction distance of 5.4 mm (Figure S6e), whereas the EMG signal is only observable at the latency earlier than 5 ms (Figure S6h). For 1 ms of pulse duration, the C-fiber volley in the ECAP waveform appears with a higher magnitude at the same latency as in previous ECAP (Figure S6f), and the EMG signal is observable only at the latency earlier than 5 ms as before (Figure S6i). This result is consistent with a previously reported value in a similar experimental setting[40], which supports our assertion that the waveform at the C-fiber

conduction velocity range is likely to be from the C-fibers in the vagus nerve for the rat VNS model.

In the future, we need to further investigate the long-term stability of the fractal microelectrode *in vivo* since the fractal design can accelerate the dissolution of Pt by the concentrated current density at the edge[30]. Here we conducted a bench top Pt dissolution test using clinically relevant stimulus parameters[51] ("Supplementary Experiments" in the Supporting information) in 1X PBS with 0.2 mg mL^{-1} of bovine serum albumin (BSA), where we found that the fractal and circle microelectrodes with or without Pt-black coating were stable after 12 h of stimulation: CSC_c (Figure S7a), E_{mc} (Figure S7b), E_{load} (Figure S7c), and atomic weight percentage of Pt and O from energy dispersive X-ray spectroscopy (EDS, Figure S8, Figure S9) show no significant difference (p>0.05, N=3, One-tailed Student's t-test) before and after 12 h of stimulation. For Pt-black coated fractal microelectrodes, we conducted inductively coupled plasma mass spectroscopy (ICP-MS) to estimate Pt dissolution rate based on the 12 h of stimulation, which is 220 ppt per day or 80 ppb per year ("Supplementary Experiments" in the Supporting information): Assuming the worst case of continuous Pt dissolution over time, the Pt-black coated fractal microelectrode may last for 12 years until the dissolved Pt reaches cytotoxic level (1 ppm[52]). A graphene coating could mitigate the dissolution of the thin Pt-layer in the fractal microelectrode for higher stimulus parameters, as presented in the previous work[37].

We also believe that there may be more efficient geometries than the Vicsek fractal presented in this work for stimulating C-fibers more effectively in terms of energy consumption and activation profile. Moreover, we need to explore a multi-contact cuff electrode with dimensions more suitable for the long-term implantation to the rat cervical vagus nerve to validate the selective stimulation of the vagus nerve by investigating the physiology in depth. Monitoring the multimodal biomarkers such as the electrocardiogram (ECG), pneumogram for respiration rate, and heart rate would tell us more information about the functional selectivity of the stimulation with the fractal microelectrode as introduced in previous studies[18,53].

Materials and Methods

Design of the thin-film device with circle/fractal microelectrodes

Thin-film devices were fabricated from platinum (Pt) and polyimide (PI) using photolithography, as described previously by Park *et al.* (2018)[30]. We designed the thin-film device with circle and fractal microelectrodes and with two larger rectangular return electrodes to be in line with the vagus nerve once the device is implanted (Figure 1c). We designed the configuration of the electrodes so that the distances between the edges of each fractal/circle microelectrode to each return electrode are equivalent (1 mm). The guide holes at the sides, which were used to secure the mid-cervical vagus nerve in position, have a diameter of 300 μm; and the distance from the guiding hole and the edge of the microelectrode/return electrode were kept at 1 mm (Figure S1). We used PI as the substrate and the insulation layer, due to its high toughness, flexibility, and biocompatibility. Figure S2 shows the fabrication process for our devices. We adopted the Vicseck fractal shape used in previous work from our group [30]: the GSA of the fractal microelectrode matches up with

that from the circle microelectrode with 100 μm of diameter (GSA approximated to 7854 μm^2). The rationale for choosing the dimensions for each microelectrode is described in the previous work by Park *et al.* (2018)[30]. Figure 1d shows the microscopic images of the device as fabricated on a silicon wafer.

Thin-film device fabrication

A 10-μm-thick PI (PI 2525, HD Microsystems, Parlin, NJ) layer was spin-coated on a 4-inch silicon wafer with a sacrificial oxide layer and cured at 300 °C to form a substrate. The PI substrate was spin-coated with a photoresist (AZ9260, MicroChem, Newton, MA, USA) and patterned with the metal layer design using a photolithography process. The traces and the electrodes were made of sputtered Pt film (100-nm-thick) on a 10-nm-thick titanium adhesion layer. The metal traces were defined using a lift-off process. A 1.5 μm thick PI (PI 2545, HD Microsystems, Parlin, NJ) layer was then spin-coated and cured to provide an insulation layer. Second photolithography was conducted to pattern the opening of electrodes and contact pads using a similar photolithography process. Third photolithography was conducted to pattern the boundaries of thin-film cuff electrodes. The boundaries were defined using a reactive ion etching (RIE) process with 50 sccm of O_2 at 100 W in 50 mTorr for 60 min. The thin-film devices were released from the wafer within 20 min using a buffered oxide etch solution. The released devices were rinsed with de-ionized (DI) water. The contact pads of the device were connected to a flexible flat cable (FFC, AWM 20624 80C 60V VW-1, uxcell, Amazon.com) by bridging the two ends with an anisotropic conductive film by heat pressing at 150 °C.

Pt-black electroplating

The surface of bare Pt was roughened by electroplating Pt-black to reduce the impedance of the microelectrodes. The plating solution was made by mixing 17.5 mM of hexachloroplatinic acid (262587, Sigma-Aldrich St. Louis, MO, USA) with 0.03 mM of lead (II) acetate trihydrate solution (316512, Sigma-Aldrich St. Louis, MO, USA). The total applied charge densities for electroplating were controlled to be equivalent for the circle and fractal microelectrodes. Electric potential between the working electrode and counter electrode was maintained to cancel the open circuit potential of the Pt microelectrodes using a potentiostat (MultiPalmsens4, PalmSens, Houten, Netherlands). The plating was stopped when the total charge density reached 2370 mC cm^{-2}, at which point the Pt started to grow out of the boundary of the pattern for both fractal and circle microelectrodes. After the electroplating, the electrodes were carefully rinsed with DI water and dried by gently blowing N_2. A scanning electron microscope (SEM) image in Figure S3b shows the surface morphology of the Pt-black: Compared to the smooth surface of bare Pt electrode (Figure S3a), Pt-black coated surface has highly roughened cauliflower-like nano morphology, which enhances electrochemical performances by increasing surface area.

Electrochemical characterization of the microelectrodes

Cyclic voltammetry (CV) was conducted in PBS (ThermoFisher Scientific, Waltham, MA, USA) using a multi-channel potentiostat (MultiPalmSens4, PalmSens, Houten, Netherlands) with the three-electrode configuration: Ag/AgCl with 3 M KCl reference electrode (RE-1CP, ALS Co. Ltd., Tokyo, Japan), 5 mm diameter graphite counter electrode, and circle/fractal

microelectrode as a working electrode. CV was measured between the potential range of −0.6 V and 0.8 V versus the reference electrode with 50 mV/s of scan rate. EIS was conducted using a potentiostat (SP-200, Bio-Logic Inc, Seyssinet-Pariset, France) with the same electrode configuration and the same solution.

Voltage transient measurements

Voltage transient measurements were performed using a stimulus isolator (BSI-1A, BAK Electronics, Inc, Umatilla, FL, USA) using a biphasic symmetric current-controlled stimulus waveform generated from a custom MATLAB (R2019b, Mathworks, Natick, MA, USA) program developed by Ward *et al.* (2015)[54], which was also used for the *in vivo* experiments. Cathodic-first biphasic current pulse with the combination of different stimulus current amplitudes (0, 0.010, 0.025, 0.050, 0.10, 0.15, 0.20, 0.25, 0.30, and 0.40 mA) at 0.5 ms or 1 ms of pulse duration were delivered between a microelectrode (circle/fractal) and a large graphite counter electrode in the PBS solution. The pulse repetition frequency and the train duration were set at 50 Hz and 1 sec respectively, which are used only for the voltage transient experiments. The current was monitored by measuring the voltage between a 1 kΩ-resistor, which was connected in series to the negative port of the simulator. A data acquisition I/O device (USB-6361, National Instruments, Austin, TX, USA) was used to connect the neural interface to a computer running the program in MATLAB R2019b.

Surgical procedure

Three rats (Sprague-Dawley, male, 385-400 g) were used for the main results of this study. All animal experiment procedures were approved by Purdue Animal Care and Use Committee (PACUC) under ethics approval number 1112000390. All animals were housed in a 12-h light/dark cycle at a constant humidity and temperature. Animals were anesthetized using isoflurane (5.0% for the induction, 0.5-2.5% for the maintenance) with O_2 (flow rate 0.3~0.5 L/min). The temperature of the animal was maintained at 35.9-37.5 °C by a heat pad. Anesthetic gas flow and temperature were controlled by an automated anesthesia system (SomnoSuite, Kent Scientific Corporation, Torrington, CT, USA). After the induction of anesthesia, the animal was placed in a supine position on the surgical frame. 0.04 mL of butorphanol tartrate (0.5-2 mg/kg butorphanol, 1x per 4 h) was injected subcutaneously through the dorsal skin of the animal as an analgesic 10 min before shaving/cleaning the surgical site and before making the first incision. The surgical site was shaved using a clipper and cleaned by scrubbing with betadine and DI water three times alternatively. A small piece of gauze was placed under the neck to support the animal and to get better access to the vagal nerves. Saline was injected subcutaneously frequently throughout the experiment to prevent dehydration (1-4 mL per h). A midline incision was made from the midpoint of the caudal ends of mandibles to the manubrium of the sternum. Blunt dissecting techniques were used to clear the pathway to the sternohyoid, omohyoid, and sternocleidomastoid muscles. The connective tissue between the right sternocleidomastoid and the omohyoid/sternohyoid was dissected carefully to locate the carotid sheath. A retractor was used to hold the sternocleidomastoid and the sternohyoid apart. The right lateral distal part of the omohyoid was carefully separated to open access space to the distal part of the carotid sheath. The vagus nerve was isolated with a blunt dissection parallel to the axial direction of the nerve using iris scissors until the separated

nerve structure was visible. Figure 4b–c show the circumferential electrode (Figure 4b) and the thin-film device with circle and fractal (Figure 4c) as implanted to the right cervical vagus nerve proximally; and a circumferential electrode for the recording of nerve activities implanted distally on the same nerve.

For the superior laryngeal transection (SLT), blunt dissection was done to the midline of the sternohyoid/sternothyroid until the trachea and larynx complex are visible (Figure S6a). Superior laryngeal nerves were located from the lateral side of the larynx complex, and we confirmed that the branches are connected to the thyroid cartilage and cricoid cartilage before the transection. For the recurrent laryngeal transection, we made transection to the caudal part by the recording cuff implantation site of the vagus nerve. For the vagotomy, the transection was done in between the stimulation cuff site and the recording cuff site.

A pair of platinum-iridium alloy (PtIr) wires (Pt10Ir-DFT®−80%Ta, OD=76.2 μm, 1 mm de-insulated, Fort Wayne Metals, Fort Wayne, IN, USA) were used to measure electromyography (EMG) from the larynx. The surgical procedure for the EMG electrode implantation was adopted from a previous study[50]. Slits were made to the lateral caudal end of the thyroid cartilage with a 22-G needle bevel side up. The PtIr wire was picked up with fine forceps and inserted into the larynx through the bevel hole of the needle (Figure S6b). Another PtIr wire was implanted with the same manner contralaterally (Figure S6c).

In vivo ECAP measurements

Commercially available cuff electrodes (FNC-400-V-R-C-2C-30, Micro-Leads, Somerville, MA, USA) were used as the circumferential electrodes in this study. The inner diameter of the cuff electrodes was 400 μm, which is 30% larger than the average diameter of the rat vagus nerve. The cuff electrode was wetted with PBS through a 27-G needle and implanted to the distal part of the vagus nerve for the recording of ECAPs. Another cuff electrode (circumferential) or a thin-film device with circle and fractal microelectrodes was implanted to the proximal part of the vagus nerve for stimulation. The cathode of the stimulating electrode pair was positioned near the + of the recording electrode pair connected to the differential amplifier. The nerve was held by two guiding holes of the thin-film device, and the position of the electrode pair was confirmed visually using a microscope. The conduction distance was measured between the cathode of the stimulation electrode pair and the anode of the recording electrode pair using a vernier caliper. The surgical cavity was flooded with warm PBS, which was replaced after each parameter sweep. ECAPs were evoked by current-controlled pulses (1 ms pulse duration) with a current amplitude range of 0-1 mA. We chose 5 Hz as the pulse repetition frequency and 10 s as the train duration. The recording electrodes were connected to an amplifier (Grass ICP511 A.C. Amplifier, Astro-Med, Inc., West Warwick, RI, USA). The output from the amplifier was filtered through a notch filter (Hum Bug Noise Eliminator, Quest Scientific, North Vancouver, BC, Canada) to attenuate 50/60 Hz noise, and fed to a DAQ board (USB-6361, National Instruments, Austin, TX, USA) for the connection to the MATLAB interface.

ECAP data analysis

We used “min()” and “max()” functions from MATLAB to identify the negative (N1) and the positive peak (P1) of the ECAP at the C-fiber conduction velocity range. Figure 4g–i show representative ECAP waveforms with positive (green markers) and negative (blue markers) peaks for all trials. We acquired the activation profile by identifying the trial-averaged peak-to-peak amplitude $|V_{pp}|$ as a function of pulse current amplitude for each stimulus. We normalized the activation profile to the maximum observed $|V_{pp}|$ in each animal to compensate for the variability of maximum recruitment between different animals. The grand mean was estimated by averaging the normalized $|V_{pp}|$ across animals. We calculated pooled standard deviation σ_p

$$\sigma_p = \sqrt{\frac{\sum (n_i - 1)\sigma_i^2}{\sum (n_i - 1)}} \tag{3}$$

where n_i is the sample size of the population I, which is a set of results from one animal per each parameter combination; and σ_i is the standard deviation of it. We used σ_p to estimate the 95% confidence interval

$$95\,\%\ \ confidence\ interval = 1.96 \times \frac{\sigma_p}{\sqrt{N-1}} \tag{4}$$

where N is the number of samples (N=3).

Biophysical modeling of the stimulation of vagus nerve with microelectrodes

Using COMSOL Multiphysics (version 5.6, COMSOL, Burlington, MA, USA), a computational model of a circle and a fractal electrode was set up as shown in Figure S4a. Circle and fractal microelectrodes had an exposed area of 7854 μm² and were separated by 830 μm spacing center-to-center. For each electrode, a bipolar stimulus was simulated with a large rectangular (157×1270 μm) return electrode separated from the stimulation electrode by 1 mm edge-to-edge. The simulation domain consisted of a 5×2×2 mm domain composed of a 543.2k element tetrahedral mesh (generated in COMSOL) with a minimum element edge length of 0.1801 μm near the electrodes (extremely fine, physics-controlled). Neumann (zero current) boundary conditions were applied at all boundaries except the electrode surfaces. For each simulation, the potential on the active electrode (cathode) was initially applied with −0.6 V against the return electrode and scaled with the total current passing from the active to the return electrode. The simulation domain had uniform conductivity (1.59 S/m). Platinum was modeled as a perfect electrical conductor for this simulation.

The resulting electric fields were exported into the ViNERS nerve modeling pipeline (Eiber et al. 2021)[55], in which a model of a rat vagus nerve (Figure S4b) was constructed by importing axon positions, diameters from segmentation of a rat vagus nerve section[56] imaged using electron microscopy (EM). The section was collected 11 mm caudal to the common carotid bifurcation, as described previously (Pelot et al. 2020)[57]. Simulated axon diameters were as measured from the EM segmentation for each axon, and ranged

from 0.23 to 1.29 μm (median: 0.76 μm) (Figure S4c). The closest distance between the outline of the nerve and the electrode surface is 2 μm. Unmyelinated axons were randomly assigned as afferent (74%) or efferent (26%), following Prechtl and Powley (1990)[11]. Using ViNERS + NEURON (version 8.0.0; (Hines and Carnevale 1997)[58], we simulated responses to extracellular stimulation (a 1 ms cathodic pulse) for a random sample of 4% of the unmyelinated axons (total 1558 simulations) in the nerve; Figure S4b shows the simulated distribution of unmyelinated axon diameters. Unmyelinated axons were simulated using the Tigerholm model (Tigerholm et al. 2014)[59]. Complete tables of model parameters are available in Eiber *et al.* (2021)[55]. For each axon, the stimulus intensity was adjusted until a 1% increase in current resulted in the generation of an action potential within 70 ms post-stimulus-onset; no axon model exhibited spontaneous emission of action potentials. The resulting axon thresholds were visualized as a function of axon location within the nerve, and stimulation levels resulting in the recruitment of 50% of unmyelinated axons were identified.

Conclusion

Here we evaluated the *in vivo* performance of microelectrodes with different shapes for VNS and showed that the Vicsek fractal microelectrode consumes less energy while activating the vagus nerve with a smaller pulse current amplitude. We designed and fabricated a device to compare the performances of the circle and the fractal microelectrodes within a subject to reduce as many neurophysiological variations as possible. We coated the microelectrodes with Pt-black to improve the charge injection limit and confirmed that fractal microelectrodes perform better in terms of CSC_C, and electrochemical impedance. The voltage transient results show that Pt-black coating greatly improves the charge injection limit and that fractal can inject 15% more charge compared to the circle. Although the stimulus parameters we used exceeded the estimated charge injection limit to activate C-fibers to an observable level in the ECAP waveforms measured from an extraneural cuff electrode, we believe this can be addressed by using different materials to enhance the charge injection limit or by using an intraneural electrode to measure the C-fiber signals evoked by stimulus parameters within the safety limit. We found that fractal microelectrodes could activate neural responses in the C-fiber conduction velocity range at 50% of the maximum recruitable level with 23% less charge per phase compared to circle microelectrodes. Moreover, fractal microelectrodes required 52% less load energy to achieve 50% nerve activation compared to circle microelectrodes.

Supplementary Material

Refer to Web version on PubMed Central for supplementary material.

Acknowledgements

This work was supported by NIH SPARC Program (OT OD023847). This work was supported in part by the National Science Foundation (United States) under Grants ECCS-1944480. JL would like to thank Min Ku Kim for the help with noise reduction; Umm E Hani Abdulla and Peter A Zoss for the assistance with the surgeries; Chris Gilpin for the assistance with the EDS analysis.

References

1. Rutecki P Anatomical, physiological, and theoretical basis for the antiepileptic effect of vagus nerve stimulation. Epilepsia 31, S1–S6 (1990).
2. Toffa DH, Touma L, Meskine TE, Bouthillier A & Nguyen DK Learnings from 30 years of reported efficacy and safety of vagus nerve stimulation (VNS) for epilepsy treatment: A critical review. Seizure (2020).
3. Krahl SE, Senanayake SS, Pekary AE & Sattin A Vagus nerve stimulation (VNS) is effective in a rat model of antidepressant action. Journal of psychiatric research 38, 237–240 (2004). [PubMed: 15003428]
4. Chakravarthy K, Chaudhry H, Williams K & Christo PJ Review of the uses of vagal nerve stimulation in chronic pain management. Current pain and headache reports 19, 54 (2015). [PubMed: 26493698]
5. Borovikova LV et al. Vagus nerve stimulation attenuates the systemic inflammatory response to endotoxin. Nature 405, 458–462 (2000). [PubMed: 10839541]
6. Koopman FA et al. Vagus nerve stimulation inhibits cytokine production and attenuates disease severity in rheumatoid arthritis. Proceedings of the National Academy of Sciences 113, 8284–8289 (2016).
7. Bonaz B et al. Chronic vagus nerve stimulation in Crohn's disease: a 6-month follow-up pilot study. Neurogastroenterology & Motility 28, 948–953 (2016). [PubMed: 26920654]
8. De Ferrari GM et al. Chronic vagus nerve stimulation: a new and promising therapeutic approach for chronic heart failure. European heart journal 32, 847–855 (2011). [PubMed: 21030409]
9. Paulon E et al. Proof of concept: short-term non-invasive cervical vagus nerve stimulation in patients with drug-refractory gastroparesis. Frontline gastroenterology 8, 325–330 (2017). [PubMed: 29067158]
10. Jänig W The integrative action of the autonomic nervous system: neurobiology of homeostasis. (Cambridge University Press, 2022).
11. Prechtl JC & Powley TL The fiber composition of the abdominal vagus of the rat. Anatomy and embryology 181, 101–115 (1990). [PubMed: 2327594]
12. Asala S & Bower A An electron microscope study of vagus nerve composition in the ferret. Anatomy and embryology 175, 247–253 (1986). [PubMed: 3826653]
13. Settell ML et al. Functional vagotopy in the cervical vagus nerve of the domestic pig: implications for the study of vagus nerve stimulation. Journal of Neural Engineering 17, 026022 (2020). [PubMed: 32108590]
14. Ben-Menachem E Vagus nerve stimulation, side effects, and long-term safety. Journal of clinical neurophysiology 18, 415–418 (2001). [PubMed: 11709646]
15. Tyler DJ & Durand DM Functionally selective peripheral nerve stimulation with a flat interface nerve electrode. IEEE Transactions on Neural Systems and Rehabilitation Engineering 10, 294–303 (2002). [PubMed: 12611367]
16. Schiefer MA et al. Selective activation of the human tibial and common peroneal nerves with a flat interface nerve electrode. Journal of neural engineering 10, 056006 (2013). [PubMed: 23918148]
17. Schiefer MA, Polasek KH, Triolo RJ, Pinault G & Tyler DJ Selective stimulation of the human femoral nerve with a flat interface nerve electrode. Journal of neural engineering 7, 026006 (2010).
18. Aristovich K et al. Model-based geometrical optimisation and in vivo validation of a spatially selective multielectrode cuff array for vagus nerve neuromodulation. Journal of Neuroscience Methods 352, 109079 (2021). [PubMed: 33516735]
19. Ahuja AK, Behrend MR, Whalen JJ, Humayun MS & Weiland JD The dependence of spectral impedance on disc microelectrode radius. IEEE Transactions on Biomedical Engineering 55, 1457–1460 (2008). [PubMed: 18390340]
20. Boehler C, Carli S, Fadiga L, Stieglitz T & Asplund M Tutorial: guidelines for standardized performance tests for electrodes intended for neural interfaces and bioelectronics. Nature protocols 15, 3557–3578 (2020). [PubMed: 33077918]

21. Sette A et al. Battery longevity of neurostimulators in Parkinson disease: a historic cohort study. Brain stimulation 12, 851–857 (2019). [PubMed: 30842036]
22. Janders M, Egert U & Stelzle M Novel thin film titanium nitride micro-electrodes with excellent charge transfer capability for cell stimulation and sensing applications. Development 4, 1 (1996).
23. Weiland JD, Anderson DJ & Humayun MS In vitro electrical properties for iridium oxide versus titanium nitride stimulating electrodes. IEEE transactions on biomedical engineering 49, 1574–1579 (2002). [PubMed: 12549739]
24. Robblee L, Lefko J & Brummer SB Activated Ir: An electrode suitable for reversible charge injection in saline solution. Journal of the Electrochemical Society 130, 731–733 (1983).
25. Cogan SF, Plante T & Ehrlich J in The 26th Annual International Conference of the IEEE Engineering in Medicine and Biology Society. 4153–4156 (IEEE).
26. Cui X & Martin DC Electrochemical deposition and characterization of poly (3, 4-ethylenedioxythiophene) on neural microelectrode arrays. Sensors and Actuators B: Chemical 89, 92–102 (2003).
27. Wilks S, Richardson-Burn S, Hendricks J, Martin D & Otto K Poly(3,4-ethylene dioxythiophene) (PEDOT) as a micro-neural interface material for electrostimulation. Frontiers in Neuroengineering 2, doi:10.3389/neuro.16.007.2009 (2009).
28. Lee YJ, Kim H-J, Do SH, Kang JY & Lee SH Characterization of nerve-cuff electrode interface for biocompatible and chronic stimulating application. Sensors and Actuators B: Chemical 237, 924–934 (2016).
29. Golestanirad L et al. Analysis of fractal electrodes for efficient neural stimulation. Frontiers in neuroengineering 6, 3 (2013). [PubMed: 23874290]
30. Park H, Takmakov P & Lee H Electrochemical Evaluations of Fractal Microelectrodes for Energy Efficient Neurostimulation. Sci Rep 8, 4375, doi:10.1038/s41598-018-22545-w (2018). [PubMed: 29531230]
31. Watterson W, Montgomery R & Taylor R Fractal electrodes as a generic interface for stimulating neurons. Scientific reports 7, 1–9 (2017). [PubMed: 28127051]
32. Watterson WJ, Montgomery RD & Taylor RP Modeling the improved visual acuity using photodiode based retinal implants featuring fractal electrodes. Frontiers in Neuroscience 12, 277 (2018). [PubMed: 29740278]
33. Ghazavi A et al. Effect of planar microelectrode geometry on neuron stimulation: Finite element modeling and experimental validation of the efficient electrode shape. Journal of Neuroscience Methods 248, 51–58 (2015). [PubMed: 25845480]
34. Wei X, Benmassaoud M, Meller M & Kuchibhatla S in 2016 38th Annual International Conference of the IEEE Engineering in Medicine and Biology Society (EMBC). 1802–1805 (IEEE).
35. Howell B & Grill WM Evaluation of high-perimeter electrode designs for deep brain stimulation. Journal of neural engineering 11, 046026 (2014). [PubMed: 25029124]
36. Cogan SF Neural stimulation and recording electrodes. Annu. Rev. Biomed. Eng 10, 275–309 (2008). [PubMed: 18429704]
37. Park H, Zhang S, Steinman A, Chen Z & Lee H Graphene prevents neurostimulation-induced platinum dissolution in fractal microelectrodes. 2D Materials 6, 035037 (2019).
38. Foutz TJ, Ackermann DM Jr, Kilgore KL & McIntyre CC Energy efficient neural stimulation: coupling circuit design and membrane biophysics. PLoS One 7, e51901 (2012). [PubMed: 23272188]
39. Gasser HS The classification of nerve fibers. (1941).
40. Chang Y-C et al. Quantitative estimation of nerve fiber engagement by vagus nerve stimulation using physiological markers. Brain stimulation 13, 1617–1630 (2020). [PubMed: 32956868]
41. McAllen RM, Shafton AD, Bratton BO, Trevaks D & Furness JB Calibration of thresholds for functional engagement of vagal A, B and C fiber groups in vivo. Bioelectronics in medicine 1, 21–27 (2018). [PubMed: 29480903]
42. Cogan SF, Garrett DJ & Green RA Electrochemical principles of safe charge injection. Neurobionics: The Biomedical Engineering of Neural Prostheses: The Biomedical Engineering of Neural Prostheses, 55–88 (2016).

43. Cogan SF, Troyk PR, Ehrlich J & Plante TD In vitro comparison of the charge-injection limits of activated iridium oxide (AIROF) and platinum-iridium microelectrodes. IEEE Transactions on Biomedical Engineering 52, 1612–1614 (2005). [PubMed: 16189975]
44. Carli S et al. Electrodeposited PEDOT: Nafion composite for neural recording and stimulation. Advanced healthcare materials 8, 1900765 (2019).
45. Cogan SF, Troyk PR, Ehrlich J, Plante TD & Detlefsen DE Potential-biased, asymmetric waveforms for charge-injection with activated iridium oxide (AIROF) neural stimulation electrodes. IEEE Transactions on Biomedical Engineering 53, 327–332 (2006). [PubMed: 16485762]
46. Qing KY, Ward MP & Irazoqui PP Burst-modulated waveforms optimize electrical stimuli for charge efficiency and fiber selectivity. IEEE transactions on neural systems and rehabilitation engineering 23, 936–945 (2015). [PubMed: 25872215]
47. Qing KY et al. B fibers are the best predictors of cardiac activity during Vagus nerve stimulation. Bioelectronic medicine 4, 1–11 (2018). [PubMed: 32232077]
48. Nicolai EN et al. Sources of off-target effects of vagus nerve stimulation using the helical clinical lead in domestic pigs. Journal of neural engineering 17, 046017 (2020). [PubMed: 32554888]
49. Yoo PB et al. High-resolution measurement of electrically-evoked vagus nerve activity in the anesthetized dog. Journal of neural engineering 10, 026003 (2013). [PubMed: 23370017]
50. Abbas A, Mughrabi IT & Zanos S in 2021 10th International IEEE/EMBS Conference on Neural Engineering (NER). 1121–1124 (IEEE).
51. Libbus I et al. Implantable vagus nerve stimulation system performance is not affected by internal or external defibrillation shocks. Journal of Interventional Cardiac Electrophysiology 63, 555–560 (2022). [PubMed: 34467496]
52. Kovach KM et al. High-throughput in vitro assay to evaluate the cytotoxicity of liberated platinum compounds for stimulating neural electrodes. Journal of neuroscience methods 273, 1–9 (2016). [PubMed: 27485087]
53. Horn CC et al. Hydrogel-based electrodes for selective cervical vagus nerve stimulation. Journal of Neural Engineering 18, 055008 (2021).
54. Ward MP et al. A flexible platform for biofeedback-driven control and personalization of electrical nerve stimulation therapy. IEEE Transactions on Neural Systems and Rehabilitation Engineering 23, 475–484 (2015). [PubMed: 25167554]
55. Eiber CD et al. Computational modelling of nerve stimulation and recording with peripheral visceral neural interfaces. Journal of neural engineering 18, 066020 (2021).
56. Havton LA, Biscola NP, Plebani E, Rajwa B, Shemonti A, Jaffey D, Powley TL, Keast JR, Lu K-H, & Dundar M . (2022).
57. Pelot NA et al. Quantified morphology of the cervical and subdiaphragmatic vagus nerves of human, pig, and rat. Frontiers in neuroscience 14, 601479 (2020). [PubMed: 33250710]
58. Hines ML & Carnevale NT The NEURON simulation environment. Neural computation 9, 1179–1209 (1997). [PubMed: 9248061]
59. Tigerholm J et al. Modeling activity-dependent changes of axonal spike conduction in primary afferent C-nociceptors. Journal of neurophysiology 111, 1721–1735 (2014). [PubMed: 24371290]
60. Branner A, Stein RB & Normann RA Selective stimulation of cat sciatic nerve using an array of varying-length microelectrodes. Journal of neurophysiology 85, 1585–1594 (2001). [PubMed: 11287482]
61. Song K-I, Park SE, Hwang D & Youn I Compact neural interface using a single multichannel cuff electrode for a functional neuromuscular stimulation system. Annals of biomedical engineering 47, 754–766 (2019). [PubMed: 30560306]
62. Caravaca A et al. A novel flexible cuff-like microelectrode for dual purpose, acute and chronic electrical interfacing with the mouse cervical vagus nerve. Journal of neural engineering 14, 066005 (2017). [PubMed: 28628030]
63. Wei XF & Grill WM Analysis of high-perimeter planar electrodes for efficient neural stimulation. Frontiers in neuroengineering 2, 15 (2009). [PubMed: 19936312]
64. Butson CR & McIntyre CC Role of electrode design on the volume of tissue activated during deep brain stimulation. Journal of neural engineering 3, 1 (2005). [PubMed: 16510937]

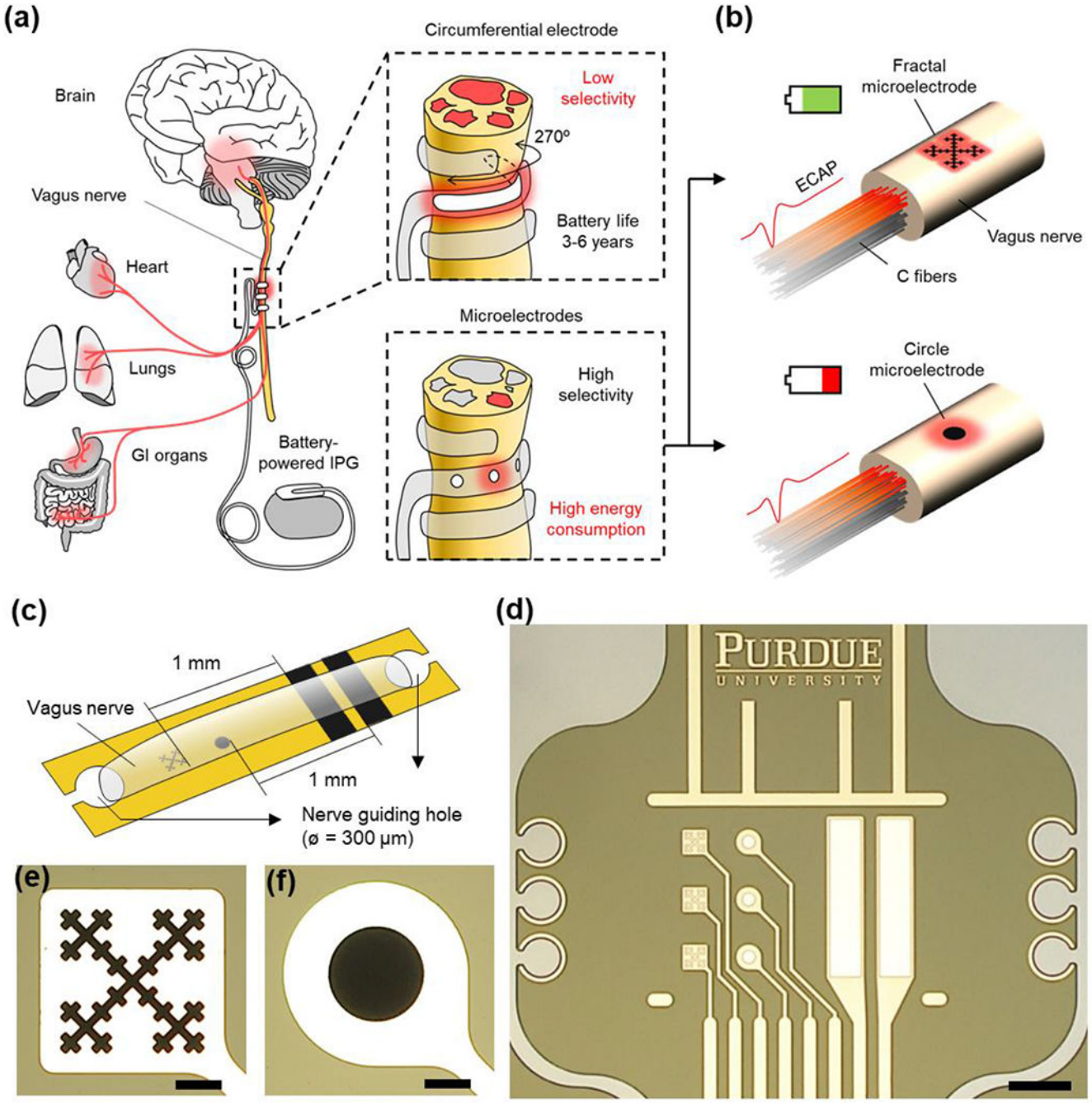

Figure 1.

Overview of the study and the device for the evaluation of the microelectrodes. (a) The conceptual illustration of using microelectrodes for a spatially selective VNS in comparison with the circumferential cuff electrode, which is conventionally used for VNS. (b) The concept of using the Vicsek fractal microelectrode toward energy-efficient selective VNS. (c) Schematic illustration of the design to compare the circle and the fractal microelectrodes in one nerve. (d) Optical microscopic images of the devices as fabricated. Scale bar: 500 μm

(e-f) Optical microscopic images of the fractal (e) and the circle (f) microelectrodes after Pt-black coating. Scale bar: 50 μm

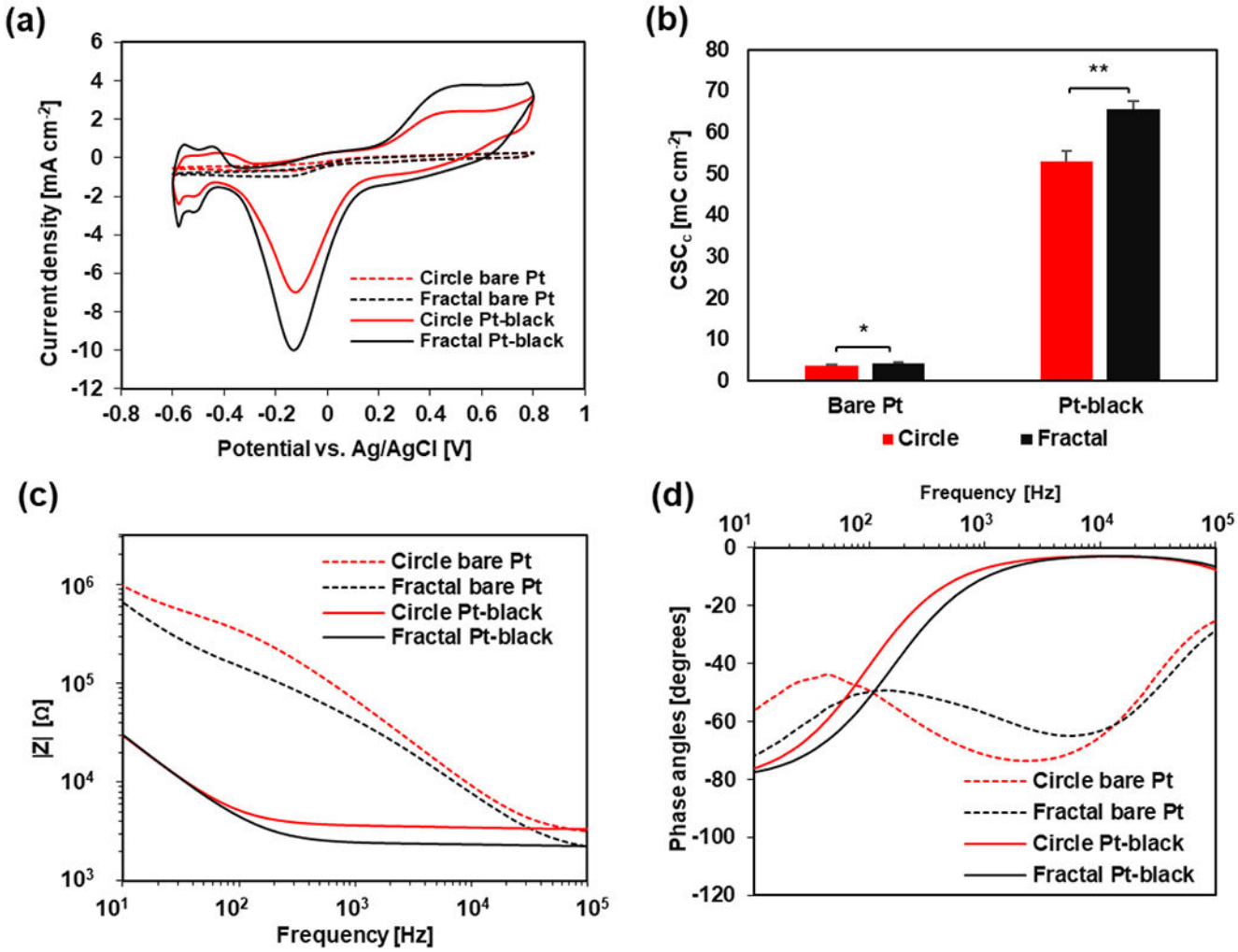

Figure 2.

Electrochemical characterization of the bare Pt and Pt-black electrode-electrolyte interface. (a) Cyclic voltammogram of each electrode type in PBS solution. (b) Cathodic charge storage capacity of the circle/fractal microelectrode with bare Pt surface (* p=0.0024, N=4); and Pt-black coated surface (** p=0.00021, N=4). (c) Bode plots from the impedance response of each type of electrode. (d) Bode plots from the phase angle responses of each type of electrode.

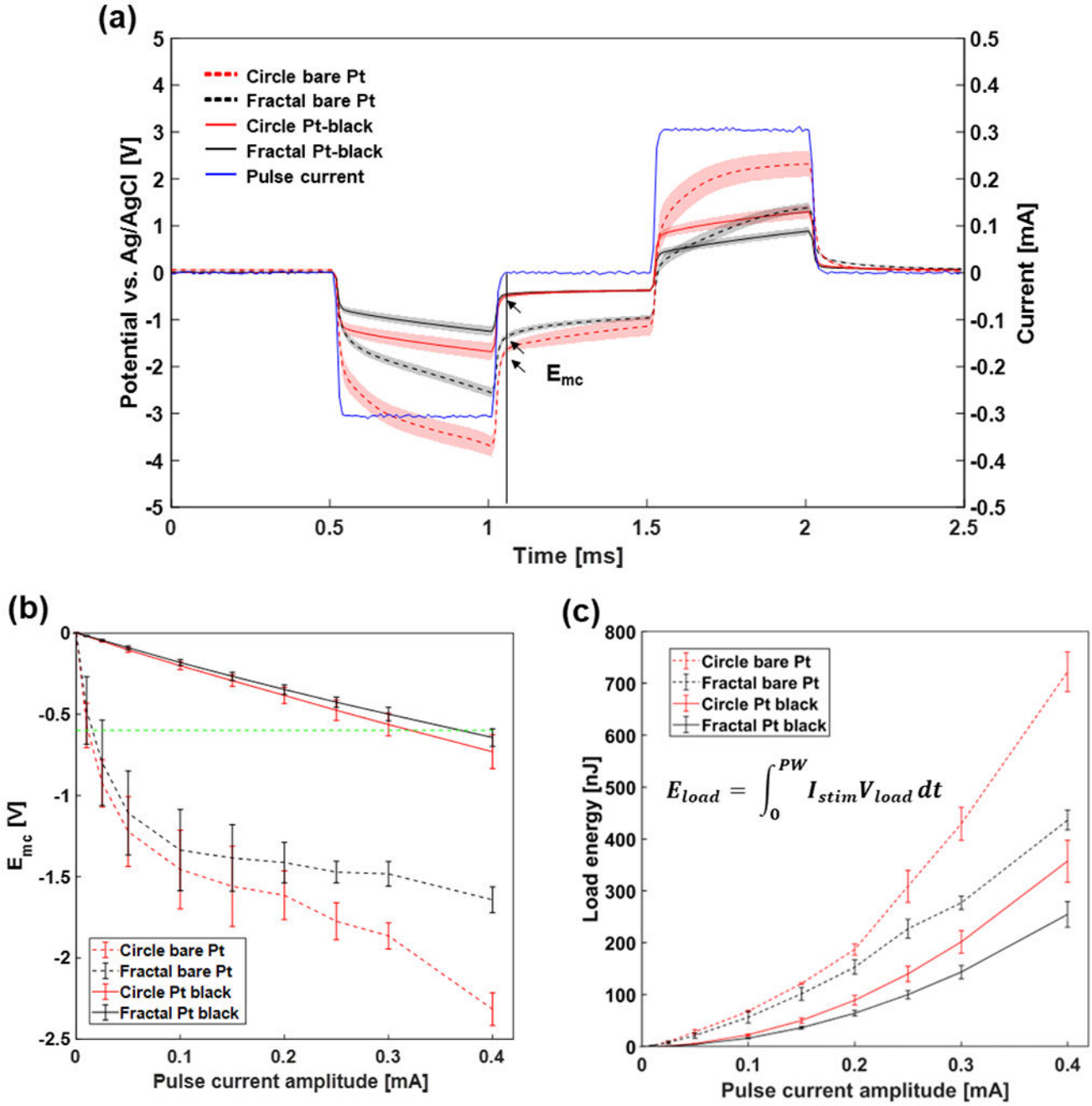

Figure 3.

Voltage transient measurements of the microelectrodes. (a) A representative plot of voltage transient response of each type of microelectrode and monitored current pulse. (b) E_{mc} profile for each type of microelectrode in PBS at 0.5 ms of pulse duration. The green dashed line indicates cathodic limit of water electrolysis (−0.6 V vs. Ag/AgCl). (c) Load energy profile for each type of microelectrode at 0.5 ms of pulse duration. *N*=4 electrodes each.

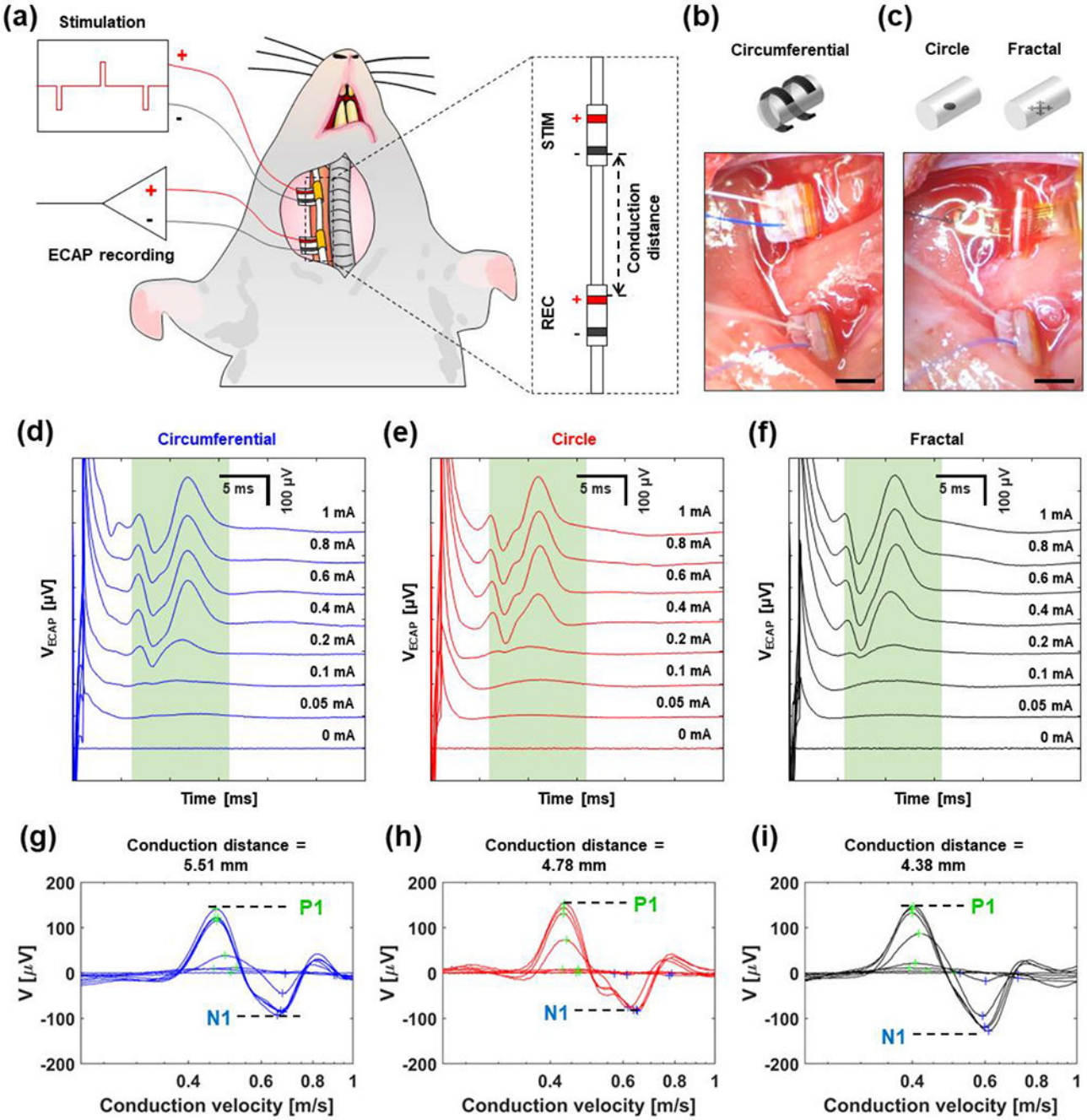

Figure 4.

In vivo experiment of VNS with different electrodes and ECAP recordings. (a) Schematic illustration of *in vivo* experiment setting. (b-c) Photographic images of the surgical cavity with the implantation of the circumferential cuff electrode (b) or the thin-film device with microelectrodes (c) for the stimulation. Scale bar: 2 mm. (d-f) Comparison of the mean ECAPs from the right cervical vagus nerve stimulated with different types of electrodes at different pulse current amplitudes in one animal (Pulse duration = 1 ms). Diphasic volleys appear at the latency between 5 ms and 15 ms (shaded green). (g-i) Diphasic volleys for

different types of electrodes plotted with respect to conduction velocity. N1: Negative peak, P1: Positive peak.

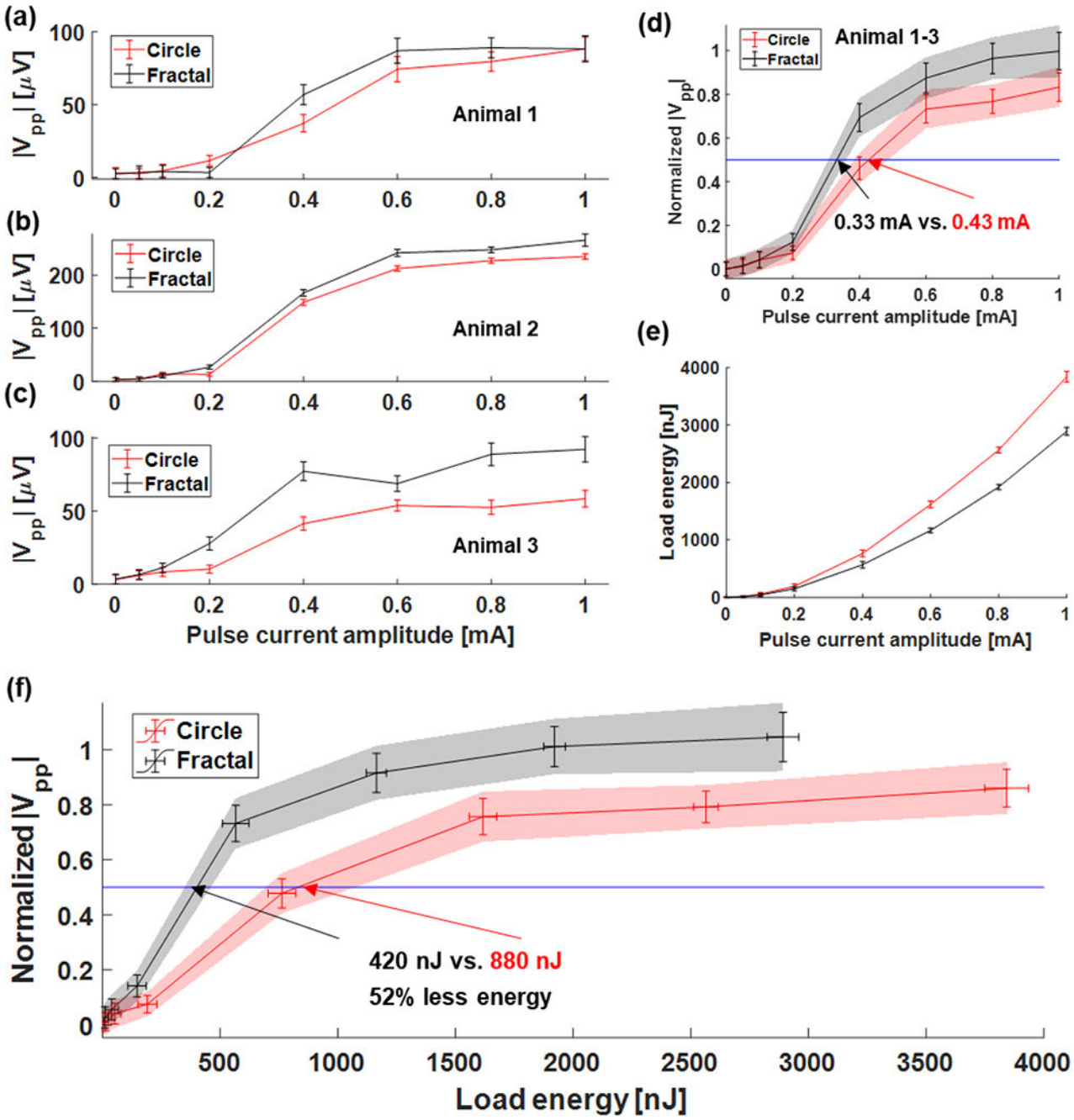

Figure 5.

Comparison of C-fiber recruitment profiles from circle and fractal microelectrodes. (a-c) Recruitment profiles of $|V_{pp}|$ from three animals at 1 ms of pulse duration. (d) Recruitment profile of normalized $|V_{pp}|$ from all three animals. Shaded regions are 95% confidence intervals for circle (red) and fractal (gray). (e) Profiles of load energy with respect to pulse current amplitude. (f) Activation profile (normalized peak-to-peak amplitude of nerve response) with respect to load energy. The intersection of each line plot to the blue line (at 0.5 of normalized $|V_{pp}|$) shows the load energy level to recruit 50% of maximum recruitable

axons from each microelectrode. Fractal microelectrodes consumed 51.99 ± 33 % (p = 0.012) less energy (424.3 ± 53 nJ) than circle microelectrodes (883.8 ± 250 nJ). Pulse duration = 1 ms.

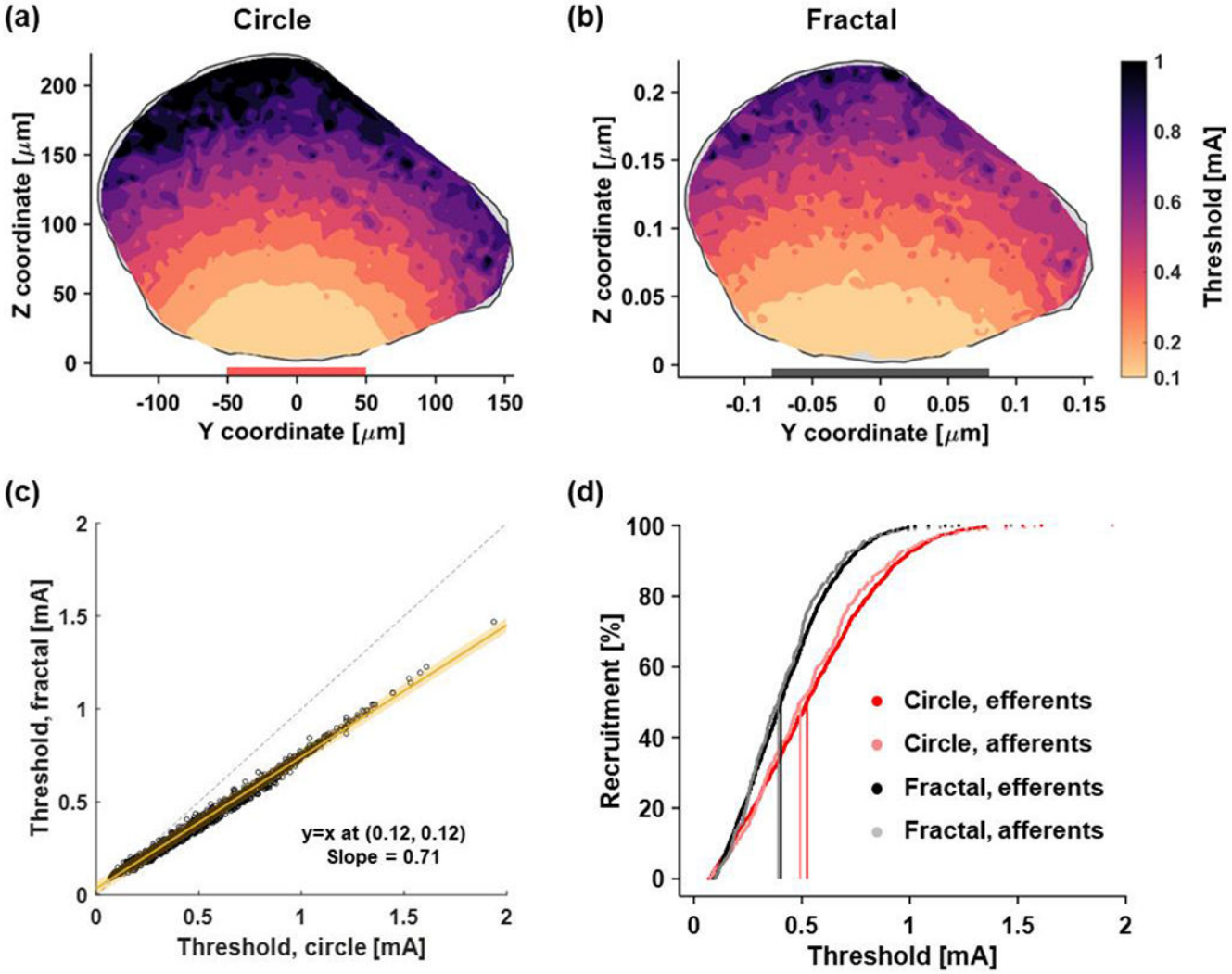

Figure 6.

Thresholds of simulated Tigerholm C-fiber model axons. (a-b) Contour plots of threshold distribution for C-fiber model axons for a circle (a) and a fractal (b) microelectrode. Red and grey rectangle annotations show the footprint extent of the circle and fractal microelectrodes, respectively. (c) Scatter plot comparing the threshold of each C-fiber axon stimulated with circle and fractal microelectrodes. (d) Modeled recruitment profile of C-fiber efferents and afferents for circle and fractal. Vertical lines indicate the threshold at 50% recruitment.

Table 1.

Studies that have shown the possibility of selective stimulation of nerve fibers

Species	Target site	Device type	Electrode material	GSA (μm^2)	Impedance at 1 kHz (kOhm)	Reference
Cat	Sciatic nerve	FINE	Pt	250000	No information	[15]
Cat	Sciatic nerve	Utah slanted electrode array (USEA), 100 electrodes	Pt plated on doped Si	5000	70-200	[60]
Rabbit	Sciatic nerve	A thin-film device with multi-contact	Pt	500000	No information	[61]
Human	Femoral nerve	FINE	Pt-Ir	196350	No information	[17]
Sheep	Vagus nerve	Silicone cuff electrode with multi-contact	PEDOT:pTS coated on the stainless steel foil	1050000	<1	[18]
Mouse	Vagus nerve	A thin-film device with multi-contact	Tungsten-Titanium	225-6400	100-910	[62]
Rat	Vagus nerve	Thin-film device	Pt-black	7854	2.4-3.6	This work (for a comparison)

Table 2.

Studies that investigated the effect of high-PSA electrodes on neural stimulation

Species	Target site	Device type	Electrode material	Electrode shape	GSA (μm^2)	PSA (mm^{-1})	Benefits	Reference
Human	Median nerve	Surface electrode	Copper	Modified Sierpinski carpet	no info	no info	22% power reduction at 50% activation compared to no-pattern	29
N/A (*in-silico*)	Not specified	Surface electrode	316L stainless steel rod	Planar disk with sinuous (serpentine) variation in the perimeter	7850000	0.4–- 1.6	Power consumption reduced by 10.1%	63
Cat	DBS, posterior internal capsule (corticobulbar axons tracts)	DBS electrode	Cr/Au	Cylindrical with Serpentine-edge design Square-edge (Rook) design	3990000–- 5985000	1.3–- 5.3	8 ± 3% (Rook shape) and 21 ± 5% (serpentine shape) power reduction at 50% activation	35
Human (*in-silico*)	DBS, Ventral intermediate nucleus of the thalamus (VIM)	DBS electrode	N/A (*in-silico*)	Cylindrical	5985000	0.79–- 1.3	The volume of tissue activated before spilling over to neighboring nuclei: 33% (0.75 mm diameter, 2.54 mm height) vs. 26% (1.27 diameter, 1.5 mm height)	64
Rat	Vagus nerve	Thin-film device	Pt-black	Vicsek fractal	7854	40 (circle), 254 (fractal)	The fractal used 51.99 % less energy at the 50% activation level compared to the circle	This work